

Direct Machine Learning Predictions of C₃ Pathways

Mingzi Sun and Bolong Huang*

The C₃ pathways of CO₂ reduction reaction (CO₂RR) lead to the generation of high-value-added chemicals for broad industrial applications, which are still challenging for current electrocatalysis. Only limited electrocatalysts have been reported with the ability to achieve C₃ products while the corresponding reaction mechanisms are highly unclear. To overcome such challenges, the first-principle machine learning (FPML) technique on graphdiyne-based atomic catalysts (GDY-ACs) is introduced to directly predict the reaction trends for the key C—C—C coupling processes and the conversions to different C₃ products for the first time. All the prediction results are obtained only based on the learning dataset constructed by density functional theory (DFT) calculation results for C₁ and C₂ pathways, offering an efficient approach to screen promising electrocatalyst candidates for varied C₃ products. More importantly, the ML predictions not only reveal the significant role of the neighboring effect and the small–large integrated cycle mechanisms but also supply important insights into the C—C—C coupling processes for understanding the competitive reactions among C₁ to C₃ pathways. This work has offered an advanced breakthrough for the complicated CO₂RR processes, accelerating the future design of novel ACs for C₃ products with high efficiency and selectivity.

energy systems, which supplies a novel method to realize the effective conversion from CO₂ to value-added chemicals.^[1] Owing to the high stability of the CO₂, the activation of CO₂ requires high energy costs to promote the multi-electron transfer processes towards varied products.^[2] The common C₁ products are widely reported in previous research including CO, HCOOH, CH₄, etc.^[1d,3] with over 90% of Faradaic efficiency (FE) during CO₂RR, which are highly important feedstocks for many industrial chemicals.^[4] Compared to the small C₁ molecules, the formation of C₂ products (ethylene, acetate, ethanol, etc.) has also been devoted great efforts to improve the selectivity and FE in recent years.^[5] Besides the Cu-based materials, many different types of electrocatalysts have been developed for realizing highly efficient conversions to C₁ and C₂ products.^[6] However, most of these electrocatalysts still require large overpotentials with applied potential <−1 V versus the reversible hydrogen electrode (RHE) to drive the

formation of C₂ products.^[7] Compared to C₂ products, the formation of C₃ products requires even more electron transfer to generate different products including acetone, propanol, and other products, which are highly valuable products for future industrial applications. Therefore, it is highly demanded to design novel electrocatalysts for the direct reduction of CO₂ to multi-carbon products with high selectivity and efficiency.

The generation of C₃ products has only been reported in limited works, and some of them rely on the electroreduction of CO to increase the overall FE. This is because CO is usually considered as one of the most important intermediates to promote the C₂ and C₂₊ products through multiple C—C coupling processes.^[8] Among different C₃ products, n-propanol is one of the most common ones, which are critical solvents and feedstocks for chemical industrial processes. Sargent et al. have reported the synthesis of open Cu nanocavity structures, which display an FE of propanol of 21 ± 1% at −0.56 V versus RHE.^[9] Meanwhile, Yang et al.^[10] designed densely packed Cu nanoparticle ensembles with structural transformation into catalytically active cube-like particles to enable the generation of n-propanol products, reaching a C₂–C₃ FE of 50% at −0.75 V versus RHE. To form C—C—C bondings, there have been different opinions about the mechanisms, where most researchers propose that couplings between C₁+C₂ intermediates are the potential pathways.^[11] Only limited in situ characterizations have proven that the coupling between C₁ and C₂ intermediates to form

1. Introduction

Currently, the global community is focusing on negative emission technologies to achieve the carbon neutrality goal and control climate change issues, which not only reduces carbon emissions but also converts carbon dioxide into highly value-added products. Carbon dioxide reduction reaction (CO₂RR) has become one of the most attractive technologies for sustainable

M. Sun, B. Huang
Department of Applied Biology and Chemical Technology
The Hong Kong Polytechnic University
Hung Hom, Kowloon, Hong Kong SAR 999077, China
E-mail: bhuang@polyu.edu.hk

B. Huang
Research Centre for Carbon-Strategic Catalysis
The Hong Kong Polytechnic University
Hung Hom, Kowloon, Hong Kong SAR 999077, China

 The ORCID identification number(s) for the author(s) of this article can be found under <https://doi.org/10.1002/aenm.202400152>

© 2024 The Authors. Advanced Energy Materials published by Wiley-VCH GmbH. This is an open access article under the terms of the [Creative Commons Attribution-NonCommercial-NoDerivs](https://creativecommons.org/licenses/by-nc-nd/4.0/) License, which permits use and distribution in any medium, provided the original work is properly cited, the use is non-commercial and no modifications or adaptations are made.

DOI: 10.1002/aenm.202400152

$\text{CH}_3\text{CH}_2\text{CHO}$ is feasible during the CO_2RR .^[12] Voiry et al. also proposed the supersaturation strategy in the highly carbonated electrolytes to realize the formation of 2-propanol from CO_2 on the CuAg alloy, where the dispersed Ag atoms weaken the binding strengths of middle carbon sites, leading to higher selectivity over 2-propanol with FE of 57%. On the other side, previous theoretical calculations also reveal that the direct CO^* coupling to form COCOCO^* is a potential reaction pathway for C_3 products on single-atom alloys.^[14] Based on current research, several key factors have been identified to influence the C_3 selectivity including the electronic structures of metal active sites, the surface engineering, and the exposed facets, etc.^[15] However, compared to the intensive research of CO_2RR towards C_1 and C_2 products, the C_3 reaction mechanisms are still unclear with limited progress, which hinders the development of efficient electrocatalysts.^[16]

Until now, different types of materials have been developed as efficient electrocatalysts for the CO_2RR process, where the generation of multi-carbon products particularly relies on Cu-based catalysts. Although previous works unravel that Cu has excellent capability to promote the C–C coupling to the production of multi-carbon chemicals, the overall FE is relatively low.^[17] The low FE and selectivity of C_3 intermediates also originated from the high energy barriers for C–C–C coupling and the competition with C_1 and C_2 products, which require much-reduced electron transfer numbers. The competing protonation of CO^* strongly suppresses the CO^* dimerization/trimerization processes towards multi-carbon products. Accordingly, increasing the selectivity from CO_2 to C_3 pathways still remains a significant challenge for current electrocatalysis. To overcome such challenges, designing electrocatalysts with favorable C_1 – C_1 – C_1 or C_1 – C_2 couplings is one of the prerequisites. As alternative electrocatalyst candidates, atomic catalysts (ACs) have the potential to realize C_3 product generation due to their high electroactivity, tunable selectivity, and maximum atom utilization efficiency.^[8,18] In particular, ACs have also displayed remarkable performances in CO_2RR .^[19] Ni ACs supported on nitrogenated graphene are reported with over 97% FE of CO at an overpotential of 0.61 V.^[20] Bao and Wang investigated the temperature-dependent CO_2RR over Fe–N–C and Ni–N–C single-atom catalysts, where the adsorption strength of intermediates and FE towards CO are optimized by temperature modulations.^[21] Deng and co-workers^[22] also reveal the Co phthalocyanines (CoPc) as a promising electrocatalyst to realize selective CO_2RR toward CO formation with 99% FE. Arrigo and co-workers^[23] also demonstrated the conversion of CO_2 to acetic acid by the Fe ACs with Fe/N–O and Fe/O–C coordination, reaching an FE of 97% and selectivity over 61%. Recently, Chen et al.^[24] have realized the generation of C_3 product acetone through the Cu ACs supported by N-doped porous carbon with FE over 36.7%, indicating the great potential of ACs for multi-carbon products.

In this work, we have carried out the first-principle machine learning (FPML) technique to perform comprehensive predictions for C_3 pathways of CO_2RR regarding the C–C–C coupling processes and reaction pathways on graphdiyne (GDY)-based ACs.^[25] This work has realized the direct predictions of C_3 pathways based on previous density functional theory (DFT) results of C_1 and C_2 pathways while no additional DFT calculations for C_3 products have been performed. For the C–C–C coupling pro-

cesses, we have considered direct C_1 coupling and C_1 + C_2 coupling based on varied reaction sites and active sites of intermediates, systematically revealing the reaction mechanisms. Based on the reaction pathways predictions, we have screened out the six most promising electrocatalysts for C_3 products including GDY-Cu, GDY-Mn, GDY-Pd, GDY-Pt, GDY-Pr, and GDY-Pm. Among the representative C_3 products, propanol is the most favored product, which is consistent with past research works, supplying important references for the reaction mechanisms. More importantly, the underlying competitions among C_1 , C_2 , and C_3 pathways as well as the key factors for C–C–C coupling processes are unraveled. Therefore, this work has supplied a novel technique to investigate the complicated and unclear C_3 pathways of CO_2RR , which will be highly beneficial for designing advanced electrocatalysts for C_3 products with improved selectivity and FE in the future.

2. Results and Discussion

Currently, theoretical calculations have achieved significant research progress for understanding the complicated CO_2RR mechanism, where our previous research has revealed the significant contributions of the neighboring effect and the small-large integrated cycle in GDY-ACs.^[26] To further probe the reaction mechanisms of C_3 pathways, the consideration of these two factors is highly necessary (Figure 1a). For the generation of C_1 products, the active sites are relatively simple since only a single active site is involved in the reaction even for different products and intermediates. As the products become more complicated with multi-carbon in the structure, the possible active sites significantly increase. For C_2 products, our previous works have revealed that both single and dual-binding configurations are feasible for intermediates.^[26a,b] In particular, there are asymmetrical binding configurations of key intermediates with dual active sites on GDY-ACs, which results in the double number of active sites in the same ACs due to the neighboring effect. As the carbon numbers in the products further increase in C_3 products, the binding configurations become more complicated with increased active sites, which is rarely discussed in previous research. Owing to the similar bond length of C–C bonds in both GDY and C_3 products, it becomes highly possible that three reaction sites contribute to the intermediate conversion processes. In this way, a comprehensive investigation of different reaction sites should be taken into account for C_3 products. The possible reaction sites include C1–C4 carbon sites, FR and NR sites, as well as Metal sites (Figure S1, Supporting Information). During the coupling processes, the multi C_1 and C_2 intermediates have three different distributions including 1) single, 2) two, and 3) three reaction sites. For the final products of C_3 intermediates, there are also three different binding configurations based on three types of active sites including 1) single, 2) dual, and 3) triple active sites. Accordingly, there are a total of 9 possible combinations by considering the possibilities of both initial reactants and final products (Figure 1b,c).

On the other side, previous research has proved that selectivity gradually decreases as the number of carbons in the products increases, where the formation of C_1 products already achieves over 90% FE while the FE of C_2 products is much lower ($\approx 60\%$).^[7] Based on the small-large integrated cycle mechanism proposed

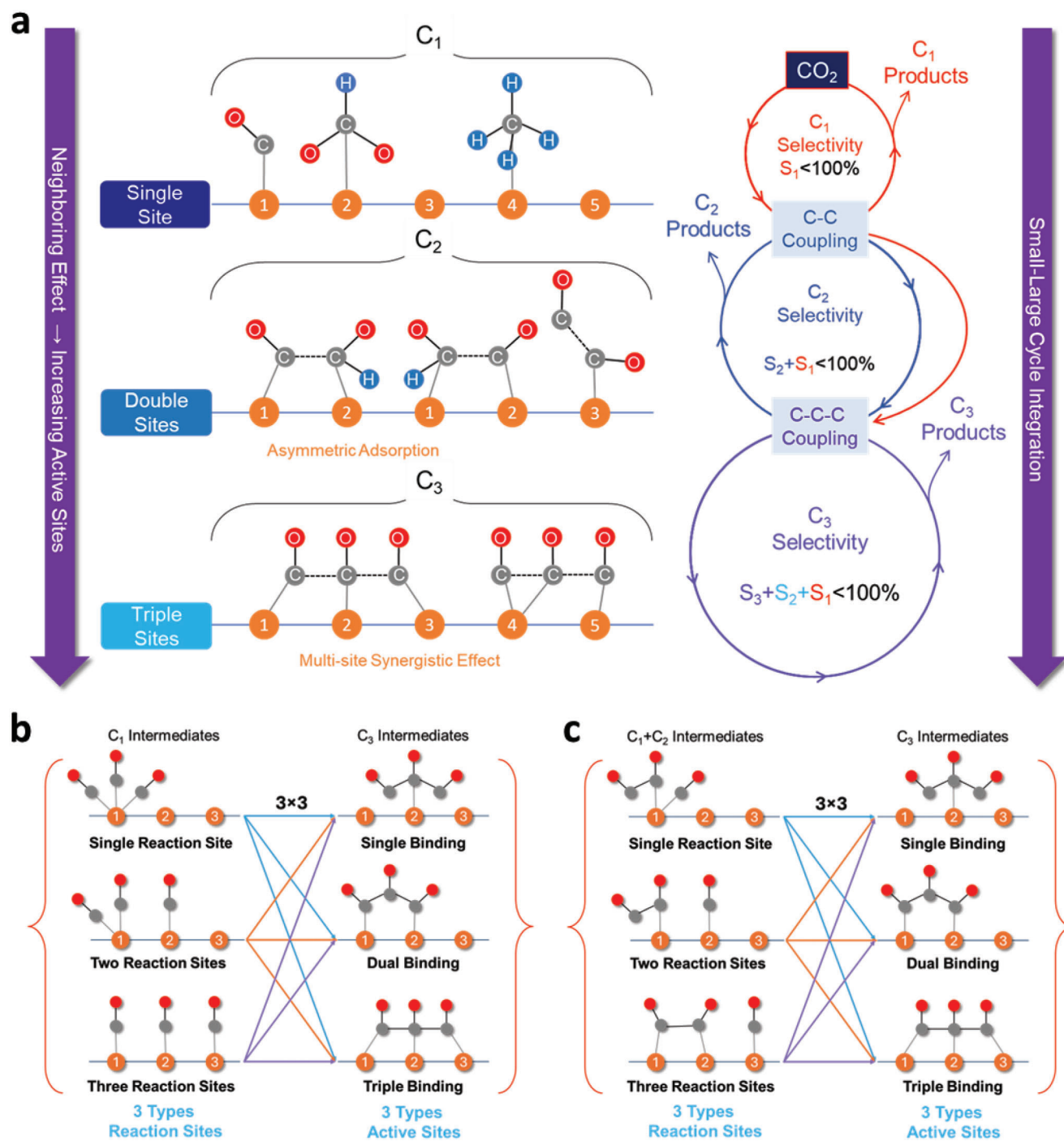


Figure 1. a) The schematic diagram for the motivations of introducing machine learning in this work. The combinations of different reaction sites and active sites for C—C—C couplings by b) C_1 intermediates and c) $C_1 + C_2$ intermediates.

in our previous work, the low FE of C_2 products is ascribed to the competition between the C_1 small cycle and C_2 medium cycle. The initiation of the C_2 medium cycle strongly relies on the C—C coupling through the C_1 key intermediate. Accordingly, the strong preference towards C_1 results in the suppression of C—C coupling and the selectivity of C_2 medium cycles. Similarly, the further increases of carbon numbers depend on the C—C—C cou-

pling, where the selectivity of the C_3 large cycle further reduces due to the competitive C_1 and C_2 cycles. To reach the C—C—C coupling for the C_3 large cycle, there are two possible ways: 1) direct jump from C_1 small cycles ($3C_1$); and 2) continuous cycle from the C_2 medium cycles ($C_1 + C_2$). By comparing these two potential reaction ways for C—C—C couplings, in-depth insights into the complicated C_3 are achieved. To comprehensively reveal

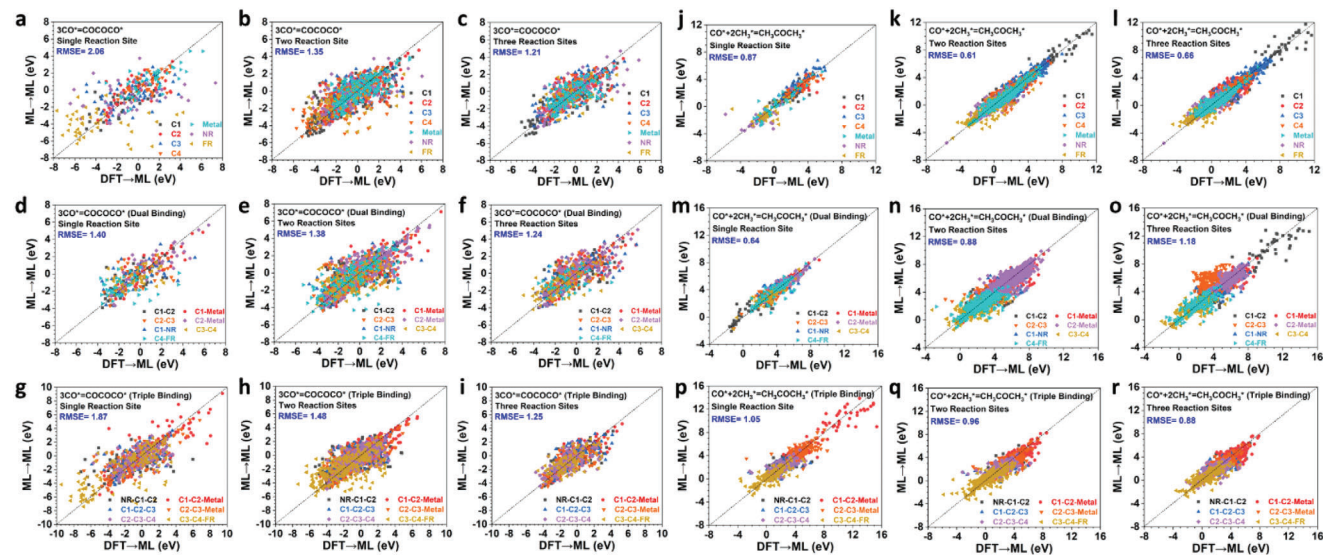


Figure 2. The direct predictions of both symmetrical and asymmetrical C—C—C couplings from C_1 intermediates. Formation of $COCOCO^*$ from a) single, b) double, and c) three reaction sites on a single active site. Formation of $COCOCO^*$ from d) single, e) two, and f) three reaction sites on dual active sites. Formation of $COCOCO^*$ from g) single, h) two, and i) three reaction sites on triple active sites. The direct predictions of symmetrical coupling to form C_3 products and key intermediates. Formation of CH_3COCH_3 from j) single, k) two, and l) three reaction sites on a single active site. Formation of CH_3COCH_3 from m) single, n) two, and o) three reaction sites on dual active sites. Formation of CH_3COCH_3 from p) single, q) two, and r) three reaction sites on triple active sites.

the reaction mechanisms of CO_2 RR for multi-carbon products, the simultaneous considerations of the neighboring effect and the small–large integrated cycle are critical. However, such investigations usually meet significant challenges due to the massive numbers of theoretical calculation models and the ultralong computation time. Our work on the comprehensive reaction pathways of C_1 and C_2 products on GDY-ACs already includes over 15 000 models. To investigate the C_3 products, simply relying on DFT calculations is not realistic to screen out potential electrocatalyst candidates of ACs. To overcome such a challenge, introducing the first principle machine learning (FPML) method becomes a promising solution since it is capable of supplying reliable predictions based on sufficient learning data sources from DFT calculations. Therefore, our data accumulations of DFT for C_1 and C_2 pathways have become feasible learning databases, which are applied in this work to realize the direct predictions of the C_3 pathways. For the ML parameters, we have selected from three different aspects including 1) physiochemical properties, 2) thermodynamic properties, and 3) structural and adsorption parameters (Table S1, Supporting Information).

For the formation of C_3 products, the C—C—C coupling is the most important step, which is also the potential rate-determining step (RDS). As the most common C_1 intermediates, the direct couplings of CO^* through the symmetrical ways are revealed (Figure 2). The reaction energy trends are compared between the DFT→ML and ML→ML to supply a reliability reference of the direct ML predictions, where the binding energies of all C_3 intermediates are obtained by ML without any additional DFT calculations. For “DFT to ML,” the thermodynamic trends are obtained by the energies of initial reactants from DFT calculations. Meanwhile, for “ML to ML,” the thermodynamic trends are obtained based on the energies of initial reactants from ML calculations. Based on the small root squared mean error (RMSE) for ML pre-

dictions, we can directly apply the proposed FPML method to reveal the reaction pathways of even more complicated C_{3+} products, offering an advanced and efficient approach for future research of CO_2 RR. For the symmetrical coupling of $3CO^*$ to directly form the $COCOCO^*$, we first demonstrate the single active sites of $COCOCO^*$ with different reaction sites (Figure 2a–c). As the reaction sites increase, the RMSE has significantly reduced, which represents the multi-reaction sites induced by the neighboring effect plays an important role in improving the prediction accuracy of ML. Interestingly, it is noted that Metal sites are not preferred active sites for C—C—C coupling since the strong CO^* binding hinders the further coupling process. In contrast, the $C1$ site is the most suitable active site with the overall lowest energy costs due to the balance between the binding strengths of CO^* and $COCOCO^*$. As the binding of $COCOCO^*$ changes to dual sites, a similar trend of decreasing RMSE is noted due to the neighboring effect (Figure 2d–f). The overall reaction energies are slightly higher than that of the single active sites. Nearly half of the reaction energies are still negative, supporting the direct coupling of CO^* is possible. However, different from the single active site, the preferences between different reaction sites are alleviated. For the triple binding of $COCOCO^*$, the RMSE of ML is slightly higher than that of the dual active sites (Figure 2g–i). This is because involving multi-binding configurations largely increases the possible combinations of active sites, which offset the neighboring effects, leading to slightly increased deviations from DFT calculations. In addition, the preferences of alkyl chains of GDY become more evident, which possess parallel active sites to stabilize the $COCOCO^*$ with the strongest reaction trends, especially the $C2$ — $C3$ — $C4$ and $C3$ — $C4$ —FR active sites. This unravels that the promotion of C—C—C coupling requires the suitable binding strengths of both CO^* and $COCOCO^*$, where the metal-related sites become less favored.

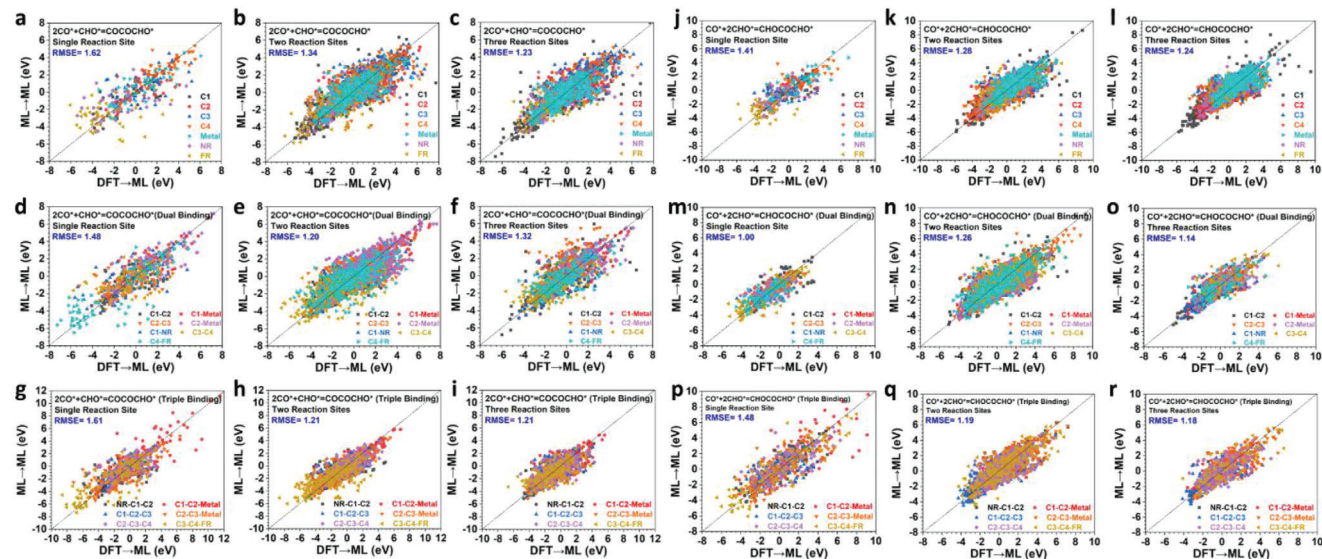


Figure 3. The asymmetrical coupling for the formation of COCOCHO* from a) single, b) two, and c) three reaction sites on a single active site. Formation of COCOCHO* from d) single, e) two, and f) three reaction sites on dual active sites. Formation of COCOCHO* from g) single, h) two, and i) three reaction sites on triple active sites. The symmetrical coupling for the formation of CHOCOCHO* from j) single, k) two, and l) three reaction sites on a single active site. Formation of CHOCOCHO* from m) single, n) two, and o) three reaction sites on dual active sites. Formation of CHOCOCHO* from p) single, q) two, and r) three reaction sites on triple active sites.

Besides the intermediates, the direct coupling of C_1 intermediates also enables the formation of key C_3 products such as acetone (CH_3COCH_3), which requires the symmetrical coupling of CO^* and CH_3^* (Figure 2j–r). For most of the reaction conditions, the direct formation of the C_3 products is not spontaneous with high energy barriers. For the single adsorption configurations, the ML has shown a high accuracy with the DFT results with evident active site preferences (Figure 3j–l). Among different sites, the Metal, NR, and FR sites are the promising active sites for the formation of the acetone with strong reaction trends while the C1–C3 sites meet high energy barriers. For acetone binding on neighboring dual sites, we notice the formation energy has increased, where most of the reaction becomes energetically unfavored, especially for the involvements of multi-reaction sites for CO^* and CH_3^* (Figure 3m–o). Only C3–C4 and C4–FR sites of limited GDY-ACs are available to proceed with the formation of acetone with spontaneous trends or with smaller energy barriers. These are attributed to the very weak binding strengths of the CH_3COCH_3 on dual active sites. Notably, the triple active site condition displays a slightly stronger reaction trend for acetone formation, where the C3–C4–FR site is the dominant active site (Figure 3p–r). Meanwhile, both C1–C2–Metal and C2–C3–Metal sites are highly unfavored for the direct C_1 couplings to form acetone due to the high energy barriers (>3 eV). These results confirm that the direct formation of C_3 products by coupling of C_1 intermediates is challenging. Therefore, bypassing the C_2 medium cycles to directly generate C_3 products is difficult, indicating that following the continuous small–medium–large cycles is more feasible for generation of C_3 products.

For the coupling of C_1 intermediates, the symmetrical and asymmetrical coupling simultaneously happens with the co-existences of CO^* and CHO^* , and the competition between these couplings still requires more investigation. First, we evaluate

the asymmetrical C–C–C coupling between CO^* and CHO^* , which shows much more possible prediction results than simple pristine CO^* couplings due to the increased reaction site combinations. For the single active site, we notice a broader reaction energy distribution than that of the symmetrical coupling (Figure 3a–c). In particular, the C1 and FR sites show the dominant contributions to the lowest reaction energy while C3 and C4 sites are not energetically preferred for the coupling process. The reaction energies of Metal sites are dependent on the specific metal elements, which exhibit large differences in the reaction trends. The numbers of dual active sites of COCOCHO* are doubled, leading to much more complicated predictions (Figure 3d–f). Under the condition of the single reaction site, the C4–FR site is the most possible active site to realize the C–C–C couplings. As more reaction sites are involved, the C3–C4 sites exhibit the lowest reaction energies while the metal-related sites show high energy barriers. Notably, the most suitable active sites are strongly related to the number of reaction sites. For all the coupling between CO^* and CHO^* in different active sites, C1–C2 and C1–NR sites become the most energetically favored active sites. For the triple active sites, the metal-related sites cannot facilitate the C–C–C coupling for COCOCHO* (Figure 3g–i). This is potentially ascribed to the steric hindrance of C1–C2–Metal and C2–C3–Metal since the three active sites are not aligned straightly, which is not beneficial for the adsorptions of multi-carbon products in long chains. In contrast, the C3–C4–NR is a highly promising active site to realize the C–C–C couplings. These results have demonstrated that direct C–C–C couplings from C_1 intermediates are not impossible, and the low selectivity of C_3 products is based on the energy barriers of the following reduction steps, unraveling that the C–C–C coupling step is not the fixed RDS for all the ACs.

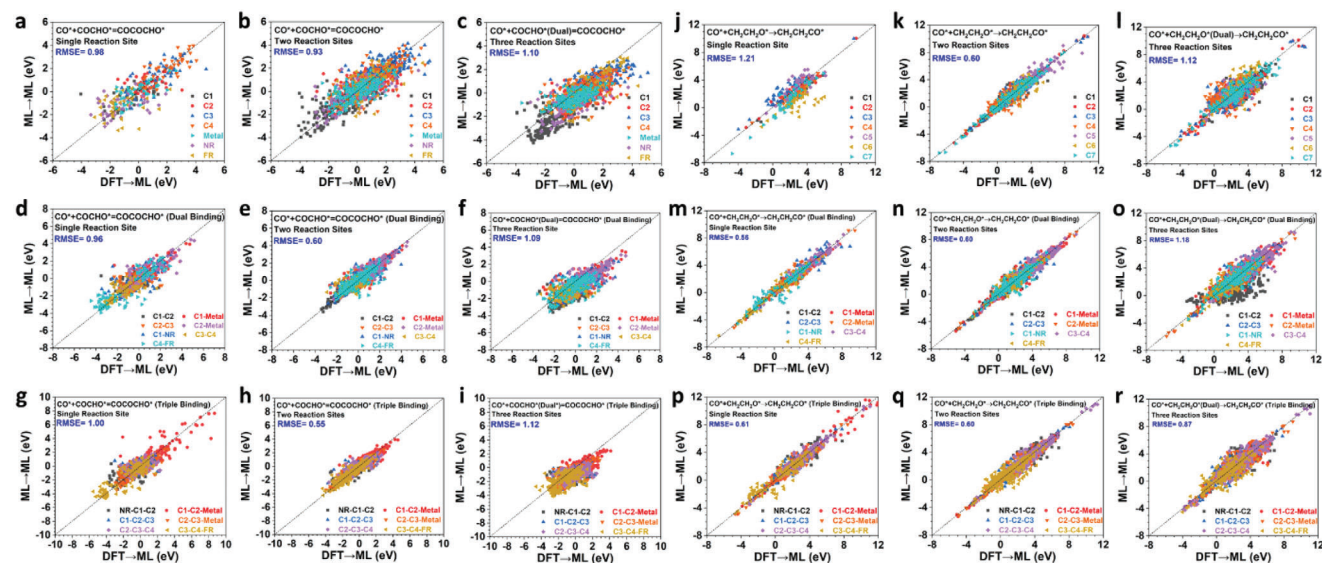


Figure 4. The direct predictions of C_1+C_2 coupling to form C_3 intermediates. Formation of $COCOCHO^*$ by CO^* and $COCHO^*$ from a) single, b) two, and c) three reaction sites on a single active site. Formation of $COCOCHO^*$ by CO^* and $COCHO^*$ from d) single, e) two, and f) three reaction sites on dual active sites. Formation of $COCOCHO^*$ by CO^* and $COCHO^*$ from g) single, h) two, and i) three reaction sites on triple active sites. The adsorptions of $COCHO^*$ are on dual active sites in (c), (f), and (i). The CO insertion into $CH_2CH_2O^*$ from j) single, k) two, and l) three reaction sites on a single active site. The CO insertion into $CH_2CH_2O^*$ from m) single, n) two, and o) three reaction sites on dual active sites. The CO insertion into $CH_2CH_2O^*$ from p) single, q) two, and (o) three reaction sites on triple active sites. The adsorptions of $CH_2CH_2O^*$ are on dual active sites in (l), (o), and (r).

Meanwhile, the symmetrical coupling of CO and CHO^* leads to the formation of $CHOCOCHO^*$, which is an important intermediate for C_3 pathways (Figure 3j–l). For the single active site, both symmetrical and asymmetrical coupling of CO and CHO^* results in similar reaction ranges, where the FR sites show the lowest reaction energies among the single reaction sites. As more reaction sites are involved, the C1 and C2 sites benefit the formation of $CHOCOCHO^*$, slightly distinct from the asymmetrical coupling with C1 and FR sites as the active sites. For the dual active sites, the screened active sites are also affected by the coupling way (Figure 3m–o). From single to triple reaction sites, the active sites gradually change from the C3–C4 site to the C1–C2 site, which is different from the symmetrical coupling with C4–FR as the dominant active site. In addition, the metal-related active sites apparently favor the symmetrical coupling over the asymmetrical coupling, confirming that different active sites lead to distinct reaction mechanisms. These differences are also demonstrated in the triple active sites (Figure 3p–r). For the single reaction sites, the C3–C4–FR sites are slightly more preferred than other sites. Most of the active sites display a broad distribution of reaction energies, indicating they are element-dependent. As the reaction energy sites increase, we notice that the C1–C2–C3 site becomes more preferred for both two and three reaction sites. These results have unraveled that the alkyl chain of GDY is more suitable for promoting the C–C–C coupling than the metal-related active sites. This is because the alkyl chain has more mild electron transfer efficiency to facilitate the coupling process rather than tightly stabilize the C_1 intermediates at the specific active sites.

By following the small–large integrated cycles, the formation of C_3 products also follows the cross-coupling of C_1+C_2 intermediates. In this case, we have investigated the reaction en-

ergy trends of CO^* and $COCHO^*$ for initiating the C_3 pathways. When CO^* and $COCHO^*$ react on the same sites or not, the similar selectivity of the active sites is revealed (Figure 4a–c). In particular, the C1, NR, and FR sites near the benzene ring of GDY are available active sites while the main alkyl chain sites (C2–C4 sites) are relatively unfavored. In comparison, the Metal sites have displayed a medium reactivity, where the reaction energies are located ≈ 0 eV in the range of -1 to 1 eV. As the $COCHO^*$ are adsorbed on dual active sites, the potential active sites maintain similar, where the edge carbon site pair is more energetically favored, especially the C4–FR sites (Figure 4d–f). It is noted that C1–C2 sites exhibit even stronger reaction trends than C4–FR sites when CO^* and $COCHO^*$ are not in the same reaction sites. As the binding site number of $COCOCHO^*$ further increases, the reaction energy ranges have not significantly changed, where the C3–C4–FR sites construct the most electroactive regions for the coupling process while the C1–C2–Metal sites meet large energy barriers for the C_3 pathway (Figure 4g–i). Compared to the C1–C2–Metal sites, C2–C3–Metal sites display a broad range of reaction energy with largely reduced energy barriers. When $COCHO^*$ is under the single binding sites, increasing the single reaction site to two reaction sites results in the decrease of RMSE, supporting the neighboring effect is beneficial for predicting the reaction trends. However, the ML prediction accuracy becomes obviously weaker when $COCHO^*$ is considered under dual active sites. These results confirm that $COCHO^*$ maintains the single adsorption configuration in practical reactions, leading to enlarged deviations in the predictions of adsorption energies with dual bindings on GDY.

Besides the direct C–C or C–C–C coupling processes, CO insertion to the C_2 intermediates is another feasible method for C_1+C_2 coupling, which has been reported as a potential

mechanism to increase the carbon chain during CO₂RR.^[27] In our work, we have selected the CO* insertion into the CH₂CH₂O* to form CH₂CH₂CO* for the formation of CH₂CH₂CO*, which is a potential intermediate for the generation of propaldehyde or propanol. Since the reaction involves the electrolyte molecules of ions and water, we have introduced the zero-point calibration strategy as proposed in our previous work and explained it as follows.^[26c] The zero-point calibration strategy has been briefly elaborated as the following equations. H₂O and OH⁻ are the main electrolyte molecules involved in CO₂ reduction reactions, which are represented by A and B, respectively. Accordingly, the formation of (OH⁻+H⁺) and (H₂O-H⁺) can be represented by (B+H⁺) and (A-OH⁻), respectively. Then, (B-A) is also represented by (A-H⁺)-(B+H⁺), leading to the following equation.

$$\Delta_1 = (A - B - 2H^+) - (B - A) = 2(A - B - H^+) \quad (1)$$

For DFT calculations, we assume the electrolyte effects induced enthalpy difference is represented by M based on the reaction of $\Delta H_A - \Delta H_B - \Delta H_{H^+} = M$. Meanwhile, the ML predicted enthalpy difference will be $\Delta H_A' - \Delta H_B' - \Delta H_{H^+}' = M'$. Accordingly, $\Delta H_A = M + \Delta H_{H^+} + \Delta H_B$ and $\Delta H_B = \Delta H_A - M - \Delta H_{H^+}$.

For the enthalpy change induced by the electrolyte molecules, there are two methods to represent the DFT calculation results as shown below.

$$\Delta_{D(1)} = \Delta H_A - \Delta H_B \quad (2)$$

$$\begin{aligned} \Delta_{D(2)} &= (M + \Delta H_{H^+} + \Delta H_B) - (\Delta H_A - M - \Delta H_{H^+}) \\ &= \Delta H_B - \Delta H_A + 2M + 2\Delta H_{H^+} \end{aligned} \quad (3)$$

When the solution is under standard hydrogen electrode (SHE) condition, the ΔH_{H^+} equals 0, leading to the following results.

$$\Delta_D = (\Delta_{D(1)} + \Delta_{D(2)})/2 = M + \Delta H_{H^+} = M \quad (4)$$

$$\Delta_{D(1)} - \Delta_{D(2)} = 2\Delta H_A - 2\Delta H_B - 2M - 2\Delta H_{H^+} = 0 \quad (5)$$

Based on the abovementioned results, the difference between DFT calculations and ML for the electrolyte effects are represented by M_D and M_{ML} , respectively. The accumulated differences between DFT and ML for the electrolyte effects are represented by $[\sum_{\min} (M_{ML} - M_D)]$, which will be zero for ideal prediction and can be further derived as follows.

$$\delta \left[\sum_{\min} (M_{ML} - M_D) \right] = 0 \quad (6)$$

$$\delta \left\{ \sum_{i=0}^N [(M_{ML} - M_D)_1 + \dots + (M_{ML} - M_D)_N] \right\} = 0 \quad (7)$$

Therefore, $M_D = M_{ML}$ = experimental constants, which indicates that the zero calibrations of the electrolyte effects are valid.

For the formation of CH₂CH₂CO* on a single active site, the corresponding reaction energies are mostly positive, revealing

the high energy costs (Figure 4j-l). This indicates that the CO insertions require the facilitation of multi-active sites to stabilize the intermediates during the dissociation of -C-O bonds. Different from other C-C-C coupling processes, the selectivity of the active sites becomes much weakened due to the broad energy distributions for all the dual active sites (Figure 4m-o). Some metal-related sites have shown highly favored reaction trends for the CO insertion, which are often considered as the less favored sites for C-C-C couplings. Moreover, the energy differences of different GDY-ACs are also much larger than other C-C-C coupling processes, which indicates that the CO insertion reaction mostly depends on the selection of the GDY-ACs. The CO insertion reaction is strongly affected by the neighboring effect, where the adsorption of CH₂CH₂CO* on the triple active sites shows the lowest RMSE (Figure 4p-r). Although the active site preferences are not as evident as other C-C-C coupling processes, it is revealed that the C3-C4-FR sites are slightly more beneficial to CO insertion.

After the predictions of different C-C-C coupling situations, we have summarized the overall reaction trends based on active sites. Notably, the Metal and nearby active sites show higher barriers for promoting the C-C-C couplings than the alkyl chain sites of GDY. For the symmetrical coupling of CO* to COCOCO*, most of the active sites are FR-dominated active sites, indicating that the suitable electroactivity and spatial arrangements of GDY are critical to promoting the formation of C₃ intermediates (Figure 5a). In comparison, the asymmetrical coupling of CO* and CHO* to generate COCOCHO* displays even lower energy barriers, revealing slightly improved preferences for symmetrical couplings (Figure 5b). Similarly, the main active site is the C3-C4-FR sites of the alkyl chains in GDY, further confirming the significance of GDY for realizing the C-C-C coupling. Compared to the asymmetrical coupling between CO* and CHO*, the selectivity of symmetrical coupling towards CHOCOCHO* becomes much weaker due to the less energetically favored reaction trends (Figure 5c). The symmetrical coupling between CO* and CH₃* to form acetone is not favored on most sites, where only the single active site of acetone is possible to promote such coupling (Figure 5d). This proves the overall very low selectivity for such couplings due to other competitive C₁ and C₂ pathways. Among different reaction sites, it is noted that most C-C-C coupling processes do not prefer the two reaction sites condition and three reaction sites are actually most preferred, which is ascribed to the potential alleviations of the steric hindrance between C₁ and C₂ intermediates (Figure 5e). Meanwhile, directly generating C₃ products such as acetone through the coupling of C₁ intermediates is strongly unfavored. The coupling of CO*+CO*+CO* and CO*+CO*+CHO* show the overall lower reaction energy, indicating that fewer hydrogen atoms involved in the coupling are more beneficial. Compared to C₁+C₂ coupling, direct C₁ coupling has stronger reaction trends, which demonstrates that the CO₂RR process is possible to directly jump from the small cycle of C₁ pathway is possible to the large cycle of C₃ pathways and bypass the medium cycle of C₂ pathways. These results have confirmed that both reaction sites and C-C-C coupling way are important in affecting the selectivity and efficiency towards C₃ products, which offers significant references to understanding the complicated reaction mechanisms of CO₂RR.

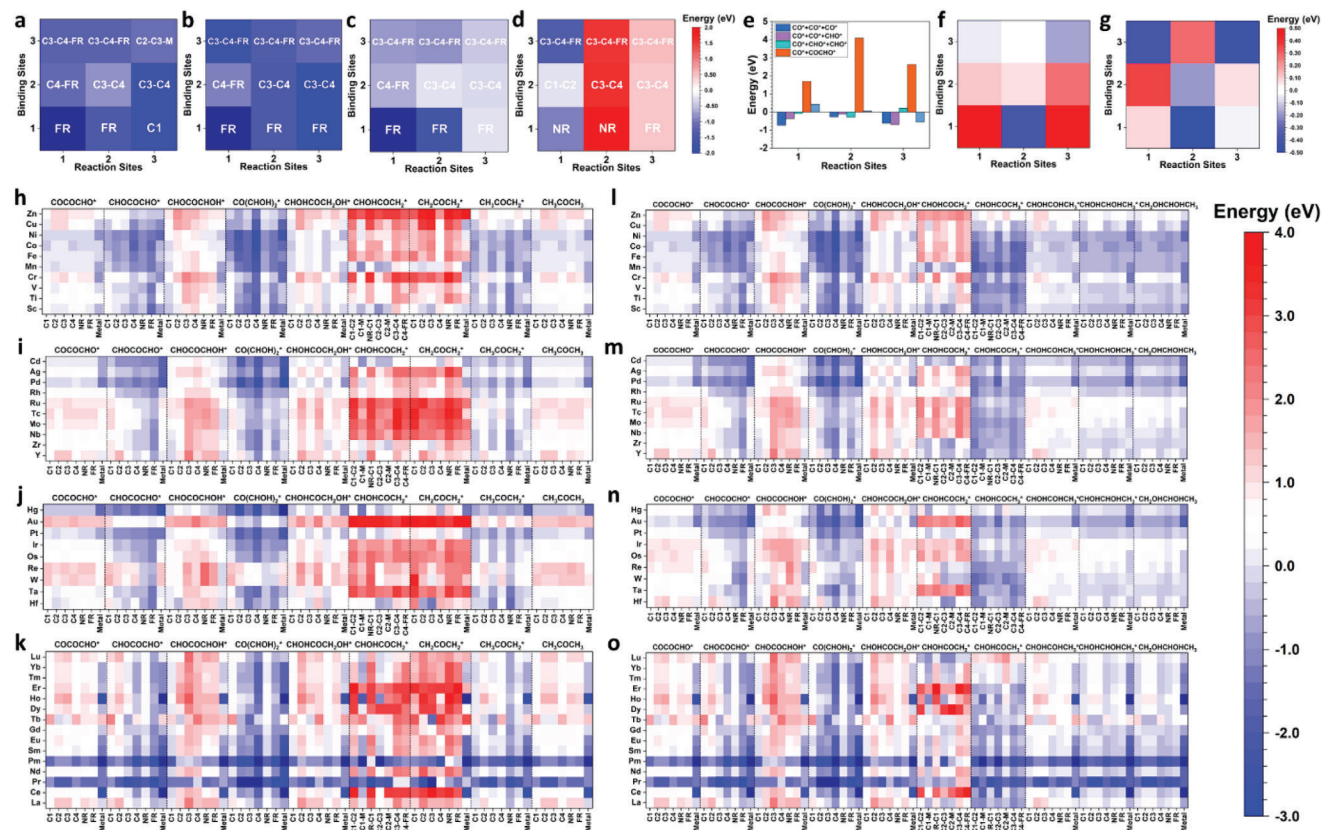


Figure 5. The average energy costs of screened active sites for promoting symmetrical and asymmetrical coupling for generation of a) COCOCHO^* , b) COCOCHO^* , c) CHOCOCHO^* , and d) $\text{CH}_3\text{COCH}_3^*$. e) The comparisons of average energy costs for C—C—C coupling processes. The competition between asymmetrical coupling towards COCOCHO^* with f) COCOCHO^* and g) CHOCOCHO^* . The reaction energy barriers of acetone for GDY-ACs are based on h) 3d, i) 4d, j) 5d, and k) Ln elements in the acidic environment. The reaction energy barriers of 1,2-propylene glycol for GDY-ACs with l) 3d, m) 4d, n) 5d, and o) Ln elements in the acidic environment.

Based on the preferences of active sites and reaction sites, we have proposed the most promising candidates for GDY-ACs for the C—C—C couplings, as shown in Table S2 (Supporting Information). For the direct coupling of CO^* to form COCOCHO^* , there is a total of 7 GDY-ACs have been identified including GDY-Ni, GDY-Cu, GDY-Pd, GDY-Pt, GDY-Hg, GDY-Pr, GDY-Pm. For the asymmetrical coupling of CO^* and CHO^* , highly similar GDY-ACs are screened. As more electrons are involved in the C—C—C couplings, the screen results of GDY-ACs change. For the symmetrical coupling of CO^* and CHO^* to form CHOCOCHO^* , the performances of GDY-Cu and GDY-Pt reduce while the other screened GDY-ACs still remain the same. In contrast, GDY-ACs show very different preferences for the symmetrical coupling between CO^* and CH_3^* , where the advantages of early TMs become evident. For 3d TMs based GDY-ACs, GDY-Sc, GDY-Ti, and GDY-V are the most suitable GDY-ACs for the formation of acetone. For 4d and 5d-based GDY-ACs, GDY-Y, GDY-Nb, GDY-Hf, and GDY-Ta are also identified for the formation of acetone. For the Ln-based GDY-ACs, the overall electroactivity is higher than GDY-TMs ACs, in which GDY-Pr and GDY-Pm display particularly excellent performances for different C—C—C coupling, supporting their great potential for C_3 pathways.

More importantly, the competitions between asymmetrical and symmetrical couplings inevitably exist during the CO_2RR ,

which are further compared regarding different reaction sites and active sites. The positive energy represents the higher preference for symmetrical coupling while the negative energy indicates the higher preference for asymmetrical coupling. Compared to COCOCHO^* formed by symmetrical coupling, we notice that the formation of COCOCHO^* displays slightly weaker preferences, especially for the single and dual active sites (Figure 5f). In contrast, the asymmetrical coupling is promoted by the triple active sites for COCOCHO^* . However, compared to the formation of CHOCOCHO^* formed by symmetrical coupling, the asymmetrical COCOCHO^* becomes more energetically preferred, which is attributed to the increases in the overall energy induced by more protons involved in the symmetrical coupling (Figure 5g). According to the results, the formation preference order is $\text{COCOCHO}^* > \text{COCOCHO}^* > \text{CHOCOCHO}^*$, where we notice that there are no absolute advantages for either symmetrical or asymmetrical coupling processes.

After revealing the C—C—C coupling processes, we have selected the representative C_3 products to investigate the reaction barriers of each step. Since the reaction mechanisms of C_3 products are highly complicated with diverse products, we have simplified the active sites of C_3 intermediates with only single and dual binding sites on GDY-ACs. All the reactions start from COCOCHO^* , where the following reduction steps are

considered with a single reaction site for easy comparisons. Acetone (CH_3COCH_3) is one of the C_3 products reported in the limited research of CO_2RR with multi-carbon products. From the COCOCO^* , we notice that there are several steps with evident energy barriers during the formation of CH_3COCH_3 in the acidic environment. For 3d transition metals (TMs) based GDY-ACs, the initial hydrogenation step towards CHOCOCHO^* is energetically preferred for most GDY-ACs (Figure 5h). The conversion from CHOCOCHO^* to CHOCOCHOH^* induces the first energy barrier, where both C1 and Metal sites are promising active sites to avoid the energy barriers. Notably, the dissociation of two $-\text{OH}$ groups from CHOHCOCHOH^* causes the largest energy barriers for acetone formation. The formation of CHOHCOCH_2 and CH_2COCH_2 causes continuous uphill reaction energies as the RDS for acetone formation. Based on the RDS steps, the GDY-Ni, GDY-Cu, GDY-Mn, and GDY-Sc are the most electroactive GDY-ACs with the smallest energy barriers, especially the C1-Metal and Metal are the main sites for RDS. Compared to 3d TMs-based GDY-ACs, the 4d TMs become less electroactive for C_3 products, where only RDS barriers are further increased (Figure 5i). In particular, we notice that Nb to Ru cannot be the metal selections of GDY-ACs for acetone formation due to the large energy barriers for all active sites. Although GDY-Cd has shown the lowest energy barriers for RDS, the toxicity of Cd prevents them from becoming the electrocatalyst candidates. Meanwhile, GDY-Pd and GDY-Zr are capable of overcoming the RDS with small energy barriers through the metal-related active sites. After the RDS, it is noted final hydrogenation steps still display a minor barrier for most of the GDY-ACs, except for the GDY-Pd and GDY-Zr, indicating them as the potential candidates for acetone formation. For the 5d TMs-based GDY-ACs, the GDY-Au is first excluded for acetone formation due to the ultrahigh energy barriers (>3.5 eV) (Figure 5j). Different from 3d TMs, both GDY-Cd and GDY-Hg show minor barriers for RDS while the GDY-Zn meets a large barrier, revealing different electroactivity for the fully occupied d orbitals of IIB group TMs. Similar to the 4d TMs-based GDY-ACs, the VIIB group TMs are potential candidates for GDY-ACs towards the acetone formation, where GDY-Pt easily overcomes the RDS through specific active sites. Compared to TMs, the overall electroactivity of lanthanide-based GDY-ACs is obviously improved since the Metal sites are highly electroactive for the continuous hydrogenation steps from COCOCO^* to CHOHCOCH_2^* (Figure 5k). We have noticed that GDY-Pm and GDY-Pr have displayed barely any barriers for all the reaction steps, even the RDS. However, since their high electroactivities have also been noticed for the C_2 products in our previous research, it is highly possible that there is strong competition and lower selectivity for both C_2 and C_3 products. Therefore, for the acetone formation, we have screened out several possible candidates through the ML direct predictions including GDY-Cu, GDY-Mn, GDY-Ni, GDY-Sc, GDY-Pd, GDY-Zr, GDY-Hf and GDY-Pt, GDY-Pm and GDY-Pr. Compared to the acidic environment, the alkaline electrolyte is less beneficial for the acetone formation, where the energy barriers become more fluctuated regarding the active sites (Figure S2, Supporting Information). Moreover, the overall energy barriers are enlarged, especially for the RDS, which further reduces the potential electrocatalyst candidates. For 4d TMs, GDY-Pd becomes unfavorable for acetone formation while the early 4d TMs-based GDY-ACs display lower barriers of RDS through the metal-

related active sites. Similar results are also revealed in 5d TMs-based GDY-ACs. In addition, the RDS of GDY-Au changes from unfavorable to energetically favored on Metal and nearby active sites for acetone formation. In contrast, there are more potential electrocatalyst candidates for lanthanide-based GDY-ACs including GDY-Er and GDY-Dy, demonstrating that electrolyte has strong influences on the electroactivity of GDY-ACs.

As another possible product for C_3 products, 1,2-propylene glycol ($\text{CH}_2\text{OHCHOHCH}_3$) shares the same reaction steps with acetone from COCOCO^* to CHOHCOCH_2^* , where the formation of both products shares the same RDS step (Figure 5l–o). Among all the reaction steps, the formation of the CHOHCOCH_2^* is the RDS while the barriers of reaction steps are alleviated when compared to acetone, indicating a stronger reaction trend for the 1,2-propylene glycol in the acidic electrolyte. It is worth mentioning that the selectivity-determining step between acetone and 1,2-propylene glycol is the conversion of CHOHCOCH_2^* , where the direct hydrogenation towards CHOHCOCH_3^* is superior to the dehydration of CHOHCOCH_2^* . These results have revealed that GDY-ACs show a higher selectivity for the 1,2-propylene glycol over the acetone. For the continuous hydrogenation of CHOHCOCH_2^* to the final product $\text{CH}_2\text{OHCHOHCH}_3$, 3d TMs-based GDY-ACs demonstrate the lowest energy barriers, supporting the highest electroactivity (Figure 5l). It is noted that GDY-ACs with early to mid 3d TMs display the strongest reaction trend. In contrast, the late 4d and 5d TMs-based GDY-ACs indicate lower energy barriers, except for GDY-Au. GDY-Pd not only exhibits the low energy barriers for RDS but also the continuous spontaneous reaction trends for the subsequent hydrogenation, making them suitable electrocatalysts for 1,2-propylene glycol generation (Figure 5m). GDY-Au still displays relatively higher energy barriers when compared to all the other GDY-ACs of 5d TMs. This is ascribed to the over-strong binding of protons, which limits the migrations of free protons during the CO_2RR and increases the barriers for hydrogenations (Figure 5n). For the Ln-based GDY-ACs, GDY-Pr and GDY-Pm still possess the obviously stronger electroactivity for the formation of 1,2-propylene glycol, which is similar to the acetone formation as well as other C_2 products, leading to the strong competition among all the products (Figure 5o). On the other side, the strong binding of C_2 and C_3 products on GDY-Pr and GDY-Pm potentially affects the conversion efficiency of CO_2RR due to the desorption barriers. Besides GDY-Pr and GDY-Pm, several other GDY-ACs are also identified with high electroactivity such as GDY-Ho. In addition, the C1-Metal sites of GDY-Ce, GDY-Nd, GDY-Sm, GDY-Eu, GDY-Dy, GDY-Tm, and GDY-Yb also promote the RDS steps with reduced energy costs than other active sites. When the electrolyte changes from acidic to alkaline, we notice that the reaction barriers are enlarged, where the formation of CHOCOCHOH^* also becomes potential RDS for GDY-ACs (Figure S3, Supporting Information). From 3d to 5d-based GDY-ACs, the RDS barriers gradually alleviated, indicating that more 5d-based GDY-ACs are suitable for the generation of 1,2-propylene glycol. For Ln-based GDY-ACs, although the reaction barriers increase, the potential candidates for CO_2RR remain similar.

Propanol is the most studied C_3 product, which requires 18 electrons to transfer from CO_2 and has been identified in previous experiments.^[10,12,13] The initial hydrogenation from

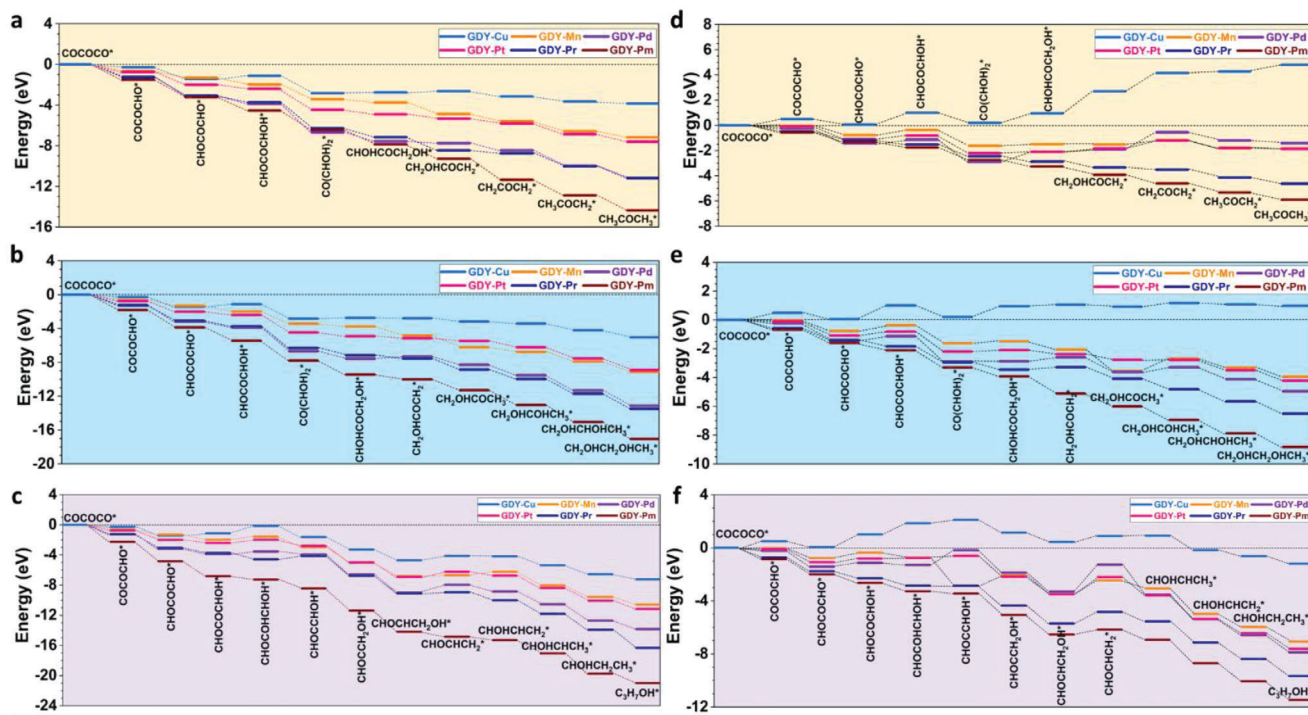


Figure 7. The reaction pathways of selected GDY-ACs for a) acetone, b) 1,2-prolyene glycol, and c) 1-propanol based on the reaction pathways with the smallest energy costs. The reaction pathways of selected GDY-ACs for d) acetone, e) 1,2-prolyene glycol, and f) 1-propanol based on the average barriers of all reaction sites.

TM-based GDY-ACs show energetically favored trends for RDS, leading to less suitable candidates for the formation of 1-propanol. The high electroactivity of GDY-Pr and GDY-Pm are also strongly weakened, where only limited active sites are able to promote the RDS, further confirming the reduced CO_2 RR performances of GDY-ACs in the alkaline environment.

According to the preliminary screening of the energy barriers directly predicted by ML, we have demonstrated the reaction energy changes of six selected GDY-ACs for the formation of different C_3 products (Figure 7a–c). All the reaction energies are obtained based on the most energetically favored active sites, which are dominated by the Metal sites. From acetone to 1,2-prolyene glycol and 1-propanol, the overall reaction energies gradually decrease, supporting the increasing reaction trends for 1-propanol with the highest selectivity as past research works. The GDY-Pm has evidently better CO_2 RR performances than all the other screened GDY-ACs, which is the most promising candidate for promoting the generation of C_3 products. During the formation of acetone, we notice that only GDY-Cu shows two minor energy barriers of 0.30 and 0.11 eV, respectively for the formation of CHOCOCHOH^* and $\text{CH}_2\text{OHCCHO}_2^*$ (Figure 7a). The GDY-Pd shows the highest electroactivity among TMs-based GDY-ACs, which is similar to that of GDY-Pr. For the generation of 1,2-prolyene glycol, the reaction steps from COCO^* to $\text{CH}_2\text{OHCCHO}_2^*$ are identical to the pathway of acetone (Figure 7b). However, compared to the acetone pathways, the selectivity to 1,2-prolyene glycol is stronger since the direct hydrogenation of $\text{CH}_2\text{OHCCHO}_2^*$ is more energetically favored than the dehydration towards acetone formation. In the generation of 1-propanol, the reaction energy further decreased for

the selected GDY-ACs (Figure 7c). Although the reaction trends become stronger, there are more reaction barriers that appear during the reaction steps. For the conversion from CHOCOCHOH to CHOCOCHOH^* , GDY-Cu, GDY-Mn, GDY-Pd, and GDY-Pd all display an energy barrier. These results reveal that the hydrogenation of $-\text{C}$ is more challenging than $-\text{O}$ due to the different electronegativity and electronic distributions. In addition, another evident barrier occurs at the dehydration of $\text{CHOHCH}_2\text{OH}^*$, which is the RDS for the 1-propanol pathway. Compared to acetone and 1,2-prolyene glycol, the GDY-Pr and GDY-Pm are more electroactive for the 1-propanol generation owing to the much-reduced reaction energies. The reaction energy changes of the selected ACs have indicated the promising C_3 selectivity of Ln-based GDY-ACs.

In addition, we have also demonstrated the average barriers of the GDY-ACs for different reaction pathways (Figure 7d–f). Notably, the average approach has alleviated the reaction trends for all the GDY-ACs towards different C_3 products. In addition, we have noticed that there are more reaction barriers appearing, indicating the significance of active sites for promoting the key reaction steps. For the overall reaction trends, the formation of 1-propanol is still higher than 1,2-prolyene glycol and acetone, representing the overall product selectivity is not significantly changed. For the generation of acetone, the conversion from CHOCOCHO^* to CHOCOCHOH^* and $\text{CH}_2\text{OHCCHO}_2$ to CH_2COCH_2 are two main barriers for most of the screened GDY-ACs (Figure 7d). In contrast, GDY-Pr and GDY-Pm still show energetically favored trends. For the production of 1,2-prolyene glycol, the hydrogenation step from CHOHCOCHOH to $\text{CHOHCOCH}_2\text{OH}$ becomes another

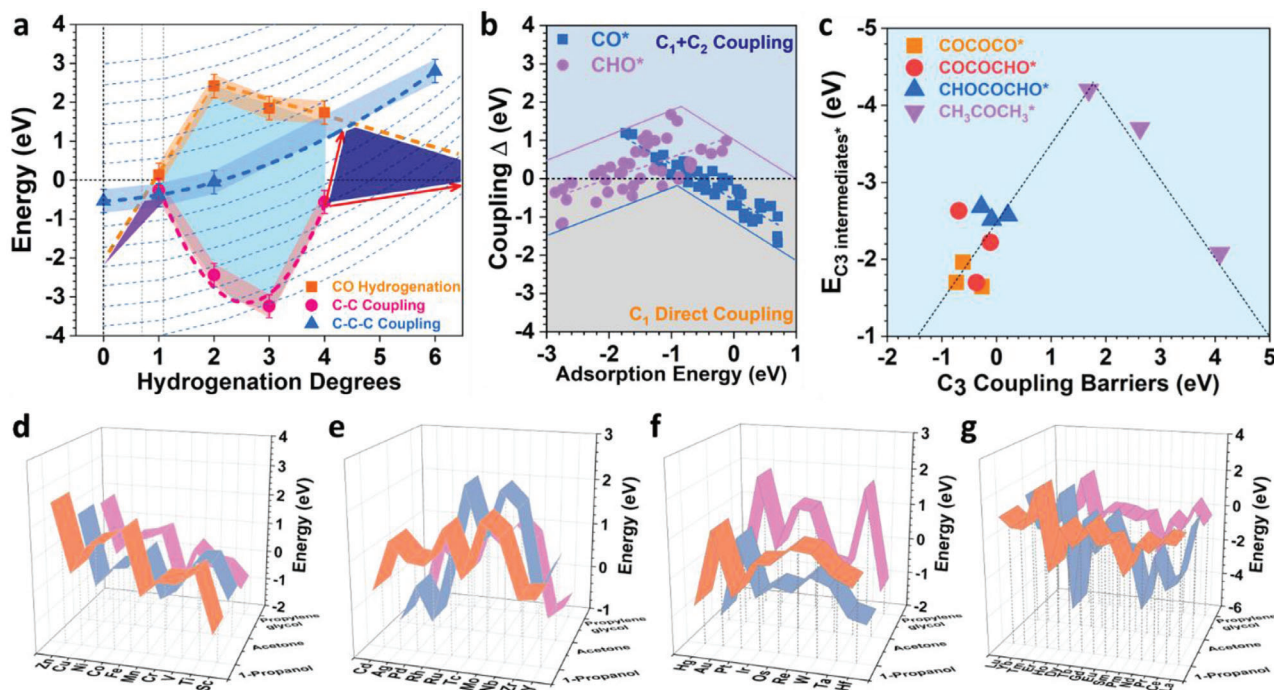


Figure 8. a) The correlation between hydrogenation degrees and coupling barriers. b) The competition between C₁ direct coupling and C₁+C₂ coupling. c) The volcano between the adsorption energies of C₃ intermediate and C—C—C coupling barriers. The triple saddle correlation between the RDS barriers and GDY-ACs with d) 3d, e) 4d, f) 5d transition metal elements. g) The converse saddle correlation between the RDS barriers and GDY-ACs with Ln elements.

evident barrier, which is slightly smaller than the hydrogenation of CHOCOCHO* (Figure 7e). This reveals that the CHOCOCHO* to CHOCOCHOH* is the potential rate-determining step (RDS) for the 1,2-prolyene glycol generation. Similarly, GDY-Pr and GDY-Pm easily overcome these RDS with overall high electroactivity for C₃ products. Although the generation of 1-propanol has the strongest reaction trends, the dehydration step of CHOCHCH₂OH to CHOCHCH₂ as the RDS shows evident barriers for all screened GDY-ACs even including GDY-Pr and GDY-Pm (Figure 7f). These average energy barriers have shown an overall electroactivity of GDY-ACs for C₃ pathways, where the contributions of active sites are important for modulating the reaction trends and reducing the barriers.

To obtain an in-depth understanding of C—C—C coupling, we have further revealed different correlations between energy barriers and different factors. CO* is one of the key intermediates, which is significant for C₁, C₂, and C₃ products through the hydrogenation or coupling processes. For direct hydrogenation processes of CO*, the average ML-predicted barriers of all GDY-ACs display a volcano trend with overall high energy barriers (Figure 8a). Meanwhile, an evident parabolic trend is identified between the C—C coupling energies and the hydrogenation degrees of the intermediate. The C—C—C coupling of C₁ intermediates also demonstrates a parabolic trend based on the quadratic equation with R² = 0.999. This indicates that the C—C—C coupling is limited by the proton numbers of three, supporting that the C—C—C couplings of C₁ intermediates usually occur between CO* and CHO* while other couplings may meet higher energy barriers. For comparisons of three different reactions of CO*, the purple shaded area indicates a very small range for the direct

C—C—C coupling by C₁ intermediates when compared to C—C couplings or direct hydrogenation. When the hydrogenation degrees exceed four, the C—C—C couplings become more energetically favored, which is realized by C₁+C₂ intermediates. These results demonstrate unique selectivity competitions among C₁, C₂, and C₃ pathways of GDY-ACs predicted by ML. The C—C—C coupling is achieved by either direct C₁ coupling or C₁+C₂ coupling, which are strongly correlated with the adsorption energies of key C₁ intermediates (Figure 8b). For CO*, the stronger adsorption strength results in higher barriers of direct C₁ coupling, and the relatively weak adsorption energies (>−1 eV) guarantee the higher selectivity of direct C₁ coupling. The adsorption energies of CHO* exhibit a converse trend, where the stronger adsorption strengths are beneficial for the C₁+C₂ coupling over direct C₁ coupling. According to these results, the direct C—C—C coupling between CO* and CHO* is realized by the strong adsorption of CHO* and weak adsorption of CO*. In addition, the volcano trends are also noted between the ML-predicted binding energies of C₃ intermediates and the C—C—C coupling barriers (Figure 8c). The over-strong adsorption strengths of C₃ intermediates such as CH₃COCH₃ also cause the high C—C—C coupling barriers. Meanwhile, the C—C—C couplings are easier for weaker adsorption strengths with adsorption energies larger than −2.5 eV, which results in the negative energy barriers for COCOCHO* and CHOCOCHO*. Besides the C—C—C couplings, the smallest RDS barriers are also correlated with different elements to screen out the most suitable GDY-ACs (Figure 8d). Notably, for TM-based GDY-ACs, the RDS barrier evolutions exhibit triple saddle trends for different C₃ products, where three minimum points are distinguished. For 3d-TMs based GDY-ACs,

GDY-Sc, GDY-Mn, and GDY-Cu have the highest electroactivity for all three C_3 products. The triple saddles of 4d-TMs-based GDY-ACs show slightly different preferences, where only the early and late TMs are screened out (Figure 8e). Compared to 3d-TMs-based GDY-ACs, the RDS barriers are increased, and the formation of 1,2-propylene glycol displays smaller barriers than acetone and 1-propanol. Based on the RDS barriers, the most promising GDY-ACs for C_3 products are GDY-Zr, GDY-Pd, and GDY-Cd. Although 5d-TMs-based GDY-ACS display a similar saddle correlation with the 4d-TMs, the smallest RDS barriers are alleviated (Figure 8f). In particular, the GDY-Hf, GDY-Pt, and GDY-Hg are identified with the highest electroactivity for C_3 products, in which the formation of acetone has the smallest RDS barriers. Meanwhile, we notice that Ln-based GDY-ACs demonstrate a converse saddle correlation between RDS barriers and f electrons (Figure 8g). As the f electron increases, three evident valley points are revealed with the smallest RDS barriers, which are GDY-Pm, GDY-Pr, and GDY-Ho, respectively. These in-depth analyses of the ML-predicted energy for C–C–C couplings and C_3 products not only have discovered the electrocatalyst candidates of CO_2RR but also have supplied significant references for understanding the reaction mechanisms toward multi-carbon products in the future.

3. Conclusion

In summary, we have performed systematic ML to predict the C–C–C coupling processes as well as the C_3 reaction pathways of CO_2RR for the first time. According to the neighboring effect and small–large integrated cycles, we have compared the C–C–C couplings through different C_1 and C_2 intermediates with consideration of single to multi-active sites. Through this work, it is noted that the direct coupling of C_1 intermediates is more energetically preferred than the C–C coupling between C_1 and C_2 intermediates, which are highly correlated with the H numbers. Although the C–C–C coupling of the C_1 intermediate is a feasible reaction pathway, the direct coupling towards C_3 products displays large energy barriers, indicating that the formation of C_3 products still needs to undergo the large C_3 cycles with gradual hydrogenation steps during the reduction. The reaction sites display most C–C–C coupling prefer single or three reaction sites while the two reaction sites only promote the formation of $CHOCOCHO^*$. Based on the reaction pathway prediction, propanol displays the higher reaction trends than acetone and 1,2-propylene glycol, supporting previous experiments. In addition, the strong correlation between coupling processes and different key factors is demonstrated to understand the C_3 reaction mechanisms. Through the reaction energy and RDS barriers, several novel GDY-ACs are screened as promising candidates to realize efficient generation of C_3 products during CO_2RR . This work will benefit the development of novel electrocatalysts to realize C_3 product generations by CO_2RR with high electroactivity and selectivity in the future.

Supporting Information

Supporting Information is available from the Wiley Online Library or from the author.

Acknowledgements

The authors gratefully acknowledge the support from the National Key R&D Program of China (2021YFA1501101), Research Grant Council of Hong Kong (15304023), the National Natural Science Foundation of China/Research Grant Council of Hong Kong Joint Research Scheme (N_PolyU502/21), National Natural Science Foundation of China/Research Grants Council (RGC) of Hong Kong Collaborative Research Scheme (CRS_PolyU504/22), the funding for Projects of Strategic Importance of The Hong Kong Polytechnic University (Project Code: 1-ZE2V), Shenzhen Fundamental Research Scheme-General Program (JCYJ20220531090807017), the Natural Science Foundation of Guangdong Province (2023A1515012219) and Departmental General Research Fund (Project Code: ZVUL) from The Hong Kong Polytechnic University. The authors also thank the support from the Research Centre for Carbon-Strategic Catalysis (RC-CSC), the Research Institute for Smart Energy (RISE), and the Research Institute for Intelligent Wearable Systems (RI-IWEAR) of the Hong Kong Polytechnic University.

Conflict of Interest

The authors declare no conflict of interest.

Data Availability Statement

The data that support the findings of this study are available from the corresponding author upon reasonable request.

Keywords

C_3 products, C–C–C coupling, machine learning, neighboring effect, small–large integrated cycles

Received: January 10, 2024
Revised: January 24, 2024
Published online: February 11, 2024

- [1] a) K. Tran, Z. W. Ulissi, *Nat. Catal.* **2018**, *1*, 696; b) M. Liu, Y. Pang, B. Zhang, P. De Luna, O. Voznyy, J. Xu, X. Zheng, C. T. Dinh, F. Fan, C. Cao, F. P. de Arquer, T. S. Safaei, A. Mepham, A. Klinkova, E. Kumacheva, T. Filleter, D. Sinton, S. O. Kelley, E. H. Sargent, *Nature* **2016**, *537*, 382; c) S. Gao, Y. Lin, X. Jiao, Y. Sun, Q. Luo, W. Zhang, D. Li, J. Yang, Y. Xie, *Nature* **2016**, *529*, 68; d) S. Nitopi, E. Bertheussen, S. B. Scott, X. Liu, A. K. Engstfeld, S. Horch, B. Seger, I. E. L. Stephens, K. Chan, C. Hahn, J. K. Norskov, T. F. Jaramillo, I. Chorkendorff, *Chem. Rev.* **2019**, *119*, 7610; e) I. Roger, M. A. Shipman, M. D. Symes, *Nat. Rev. Chem.* **2017**, *1*, 0003; f) Z. W. Seh, J. Kibsgaard, C. F. Dickens, I. Chorkendorff, J. K. Norskov, T. F. Jaramillo, *Science* **2017**, *355*, aad4998; g) H. Xin, L. Lin, R. Li, D. Li, T. Song, R. Mu, Q. Fu, X. Bao, *J. Am. Chem. Soc.* **2022**, *144*, 4874.
- [2] Z. Zhang, X. Huang, Z. Chen, J. Zhu, B. Endrodi, C. Janaky, D. Deng, *Angew. Chem., Int. Ed.* **2023**, *62*, 202302789.
- [3] a) J. Qiao, Y. Liu, F. Hong, J. Zhang, *Chem. Soc. Rev.* **2014**, *43*, 631; b) L.-S. Zhan, Y.-C. Wang, M.-J. Liu, X. Zhao, J. Wu, X. Xiong, Y.-P. Lei, *Rare Met.* **2022**, *42*, 806; c) S. Zhang, X.-T. Gao, P.-F. Hou, T.-R. Zhang, P. Kang, *Rare Met.* **2021**, *40*, 3117.
- [4] a) F. Jiao, J. Li, X. Pan, J. Xiao, H. Li, H. Ma, M. Wei, Y. Pan, Z. Zhou, M. Li, S. Miao, J. Li, Y. Zhu, D. Xiao, T. He, J. Yang, F. Qi, Q. Fu, X. Bao, *Science* **2016**, *351*, 1065; b) F. Jiao, B. Bai, G. Li, X. Pan, Y. Ye, S. Qu, C. Xu, J. Xiao, Z. Jia, W. Liu, T. Peng, Y. Ding, C. Liu, J. Li, X. Bao, *Science* **2023**, *380*, 727.

- [5] H. Tabassum, X. Yang, R. Zou, G. Wu, *Chem Catalys.* **2022**, *2*, 1561.
- [6] a) J. Ding, H. Bin Yang, X.-L. Ma, S. Liu, W. Liu, Q. Mao, Y. Huang, J. Li, T. Zhang, B. Liu, *Nat. Energy* **2023**, *8*, 1386; b) H. Peng, R. Guo, H. Lin, *J. Rare Earths* **2020**, *38*, 1297; c) B. Li, F. Wang, K. Li, P. Ning, M. Chen, C. Zhang, *J. Rare Earths* **2023**, *41*, 926; d) Q. Li, Y.-C. Wang, J. Zeng, X. Zhao, C. Chen, Q.-M. Wu, L.-M. Chen, Z.-Y. Chen, Y.-P. Lei, *Rare Met.* **2021**, *40*, 3442.
- [7] a) A. Loiudice, P. Lobaccaro, E. A. Kamali, T. Thao, B. H. Huang, J. W. Ager, R. Buonsanti, *Angew. Chem., Int. Ed.* **2016**, *55*, 5789; b) H. Mistry, A. S. Varela, C. S. Bonifacio, I. Zegkinoglou, I. Sinev, Y. W. Choi, K. Kisslinger, E. A. Stach, J. C. Yang, P. Strasser, B. R. Cuenya, *Nat. Commun.* **2016**, *7*, 12123.
- [8] A. R. Woldu, Z. L. Huang, P. X. Zhao, L. S. Hu, D. Astruc, *Coord. Chem. Rev.* **2022**, *454*, 214340.
- [9] T.-T. Zhuang, Y. Pang, Z.-Q. Liang, Z. Wang, Y. Li, C.-S. Tan, J. Li, C. T. Dinh, P. De Luna, P.-L. Hsieh, T. Burdyny, H.-H. Li, M. Liu, Y. Wang, F. Li, A. Proppe, A. Johnston, D.-H. Nam, Z.-Y. Wu, Y.-R. Zheng, A. H. Ip, H. Tan, L.-J. Chen, S.-H. Yu, S. O. Kelley, D. Sinton, E. H. Sargent, *Nat. Catal.* **2018**, *1*, 946.
- [10] D. Kim, C. S. Kley, Y. Li, P. Yang, *Proc. Natl. Acad. Sci. USA* **2017**, *114*, 10560.
- [11] a) H. Xiao, T. Cheng, W. A. Goddard 3rd, *J. Am. Chem. Soc.* **2017**, *139*, 130; b) K. P. Kuhl, E. R. Cave, D. N. Abram, T. F. Jaramillo, *Energy Environ. Sci.* **2012**, *5*, 7050.
- [12] E. L. Clark, A. T. Bell, *J. Am. Chem. Soc.* **2018**, *140*, 7012.
- [13] K. Qi, Y. Zhang, N. Onofrio, E. Petit, X. Cui, J. Ma, J. Fan, H. Wu, W. Wang, J. Li, J. Liu, Y. Zhang, Y. Wang, G. Jia, J. Wu, L. Lajaunie, C. Salameh, D. Voiry, *Nat. Catal.* **2023**, *6*, 319.
- [14] L. Chen, C. Tang, Y. Zheng, E. Skúlason, Y. Jiao, *J. Mater. Chem. A* **2022**, *10*, 5998.
- [15] a) C. W. Li, J. Ciston, M. W. Kanan, *Nature* **2014**, *508*, 504; b) J. Li, F. Che, Y. Pang, C. Zou, J. Y. Howe, T. Burdyny, J. P. Edwards, Y. Wang, F. Li, Z. Wang, P. De Luna, C. T. Dinh, T. T. Zhuang, M. I. Saidaminov, S. Cheng, T. Wu, Y. Z. Finrock, L. Ma, S. H. Hsieh, Y. S. Liu, G. A. Botton, W. F. Pong, X. Du, J. Guo, T. K. Sham, E. H. Sargent, D. Sinton, *Nat. Commun.* **2018**, *9*, 4614; c) M. Jouny, W. Luc, F. Jiao, *Nat. Catal.* **2018**, *1*, 748.
- [16] a) C. Peng, G. Luo, J. Zhang, M. Chen, Z. Wang, T. K. Sham, L. Zhang, Y. Li, G. Zheng, *Nat. Commun.* **2021**, *12*, 1580; b) X. Wang, P. Ou, A. Ozden, S.-F. Hung, J. Tam, C. M. Gabardo, J. Y. Howe, J. Sisler, K. Bertens, F. P. García de Arquer, R. K. Miao, C. P. O'Brien, Z. Wang, J. Abed, A. S. Rasouli, M. Sun, A. H. Ip, D. Sinton, E. H. Sargent, *Nat. Energy* **2022**, *7*, 170.
- [17] Y. Hori, R. Takahashi, Y. Yoshinami, A. Murata, *J. Phys. Chem. B* **1997**, *101*, 7075.
- [18] a) J. Shan, C. Ye, Y. Jiang, M. Jaroniec, Y. Zheng, S. Z. Qiao, *Sci. Adv.* **2022**, *8*, eabo0762; b) Y. Chen, S. Ji, C. Chen, Q. Peng, D. Wang, Y. Li, *Joule* **2018**, *2*, 1242; c) P. Saha, S. Amanullah, A. Dey, *Acc. Chem. Res.* **2022**, *55*, 134; d) D. Gao, T. Liu, G. Wang, X. Bao, *ACS Energy Lett.* **2021**, *6*, 713; e) Y. Wang, J. Mao, X. Meng, L. Yu, D. Deng, X. Bao, *Chem. Rev.* **2019**, *119*, 1806.
- [19] N. Zhang, X. Zhang, L. Tao, P. Jiang, C. Ye, R. Lin, Z. Huang, A. Li, D. Pang, H. Yan, Y. Wang, P. Xu, S. An, Q. Zhang, L. Liu, S. Du, X. Han, D. Wang, Y. Li, *Angew. Chem., Int. Ed.* **2021**, *60*, 6170.
- [20] H. B. Yang, S.-F. Hung, S. Liu, K. Yuan, S. Miao, L. Zhang, X. Huang, H.-Y. Wang, W. Cai, R. Chen, J. Gao, X. Yang, W. Chen, Y. Huang, H. M. Chen, C. M. Li, T. Zhang, B. Liu, *Nat. Energy* **2018**, *3*, 140.
- [21] L. Lin, H. Li, Y. Wang, H. Li, P. Wei, B. Nan, R. Si, G. Wang, X. Bao, *Angew. Chem., Int. Ed.* **2021**, *60*, 26582.
- [22] Z. Zhang, J. Xiao, X. J. Chen, S. Yu, L. Yu, R. Si, Y. Wang, S. Wang, X. Meng, Y. Wang, Z. Q. Tian, D. Deng, *Angew. Chem., Int. Ed.* **2018**, *57*, 16339.
- [23] C. Genovese, M. E. Schuster, E. K. Gibson, D. Gianolio, V. Posligua, R. Grau-Crespo, G. Cibin, P. P. Wells, D. Garai, V. Solokha, S. Krick Calderon, J. J. Velasco-Velez, C. Ampelli, S. Perathoner, G. Held, G. Centi, R. Arrigo, *Nat. Commun.* **2018**, *9*, 935.
- [24] K. Zhao, X. Nie, H. Wang, S. Chen, X. Quan, H. Yu, W. Choi, G. Zhang, B. Kim, J. G. Chen, *Nat. Commun.* **2020**, *11*, 2455.
- [25] a) M. Sun, A. W. Dougherty, B. Huang, Y. Li, C. H. Yan, *Adv. Energy Mater.* **2020**, *10*, 1903949; b) M. Sun, T. Wu, A. W. Dougherty, M. Lam, B. Huang, Y. Li, C. H. Yan, *Adv. Energy Mater.* **2021**, *11*, 2003796; c) M. Sun, H. H. Wong, T. Wu, A. W. Dougherty, B. Huang, *Adv. Energy Mater.* **2021**, *11*, 2101404.
- [26] a) M. Sun, H. H. Wong, T. Wu, A. W. Dougherty, B. Huang, *Adv. Energy Mater.* **2022**, *12*, 2103781; b) M. Sun, H. H. Wong, T. Wu, Q. Lu, L. Lu, C. H. Chan, B. Chen, A. W. Dougherty, B. Huang, *Adv. Energy Mater.* **2022**, *13*, 2203858; c) M. Sun, B. Huang, *Adv. Energy Mater.* **2023**, *13*, 2301948; d) M. Sun, B. Huang, *Nano Energy* **2022**, *99*, 107398.
- [27] a) S. Lee, G. Park, J. Lee, *ACS Catal.* **2017**, *7*, 8594; b) T. Jaster, A. Gawel, D. Siegmund, J. Holzmann, H. Lohmann, E. Klemm, U. P. Apfel, *iScience* **2022**, *25*, 104010.